ACS APPLIED NANO MATERIALS

www.acsanm.org Article

High-Responsivity UV Photodetectors Based on High-Mobility Graphene Epitaxially Grown on 4H-SiC

Xue Wang, Cao Tang, Rui Li, Xiaodong Zhu, Wei Jin, Luzhen Hao, Rongke Sun, Jinwei Liu, Yanqing Ma,* and Lei Ma*

Cite This: *ACS Appl. Nano Mater.* 2025, 8, 15799–15807 Read Online

ABSTRACT: Achieving outstanding detection performance with a simple detector construction has long been one of the goals of photodetector development. In this study, we report a high-responsivity graphene/silicon carbide (Gr/SiC) ultraviolet (UV) photodetector consisting of a monolayer of graphene grown epitaxially on the silicon surface of SiC. By optimizing the growth process, the carrier mobility of the monolayer graphene with a large area of 3.5 × 4.5 mm^2 was achieved up to 3020.54 $cm^2/(V \cdot s)$. Under UV irradiation of 0.004 μW at 275 nm, the Gr/SiC photodetector achieves a high responsivity of 5425 A/W, which is 1 order of magnitude higher than the 254.1 A/W of the best responsivity of reported Gr/SiC UV detectors. Meanwhile, the photoconductive gain of the photodetector reaches 24462, which is nearly 50 times the highest photoconductive gain of 490.8 among reported Gr/SiC UV detectors. This outstanding performance is driven by the excellent carrier mobility of the epitaxial graphene, which enables the photogenerated carriers to rapidly migrate to the electrodes, thus significantly improving the photoconductive gain of the detector. At the same time, the simplified preparation process greatly reduces the cost, shortens the production cycle, and improves the feasibility of mass production, which provides crucial support for the industrial application of high-responsivity UV photodetectors.

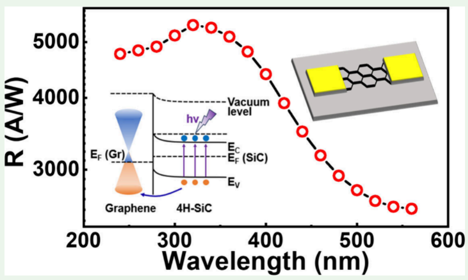

KEYWORDS: *silicon carbide epitaxial graphene, UV photodetector, photoconductivity, responsivity, gain*

■ INTRODUCTION

In modern society, high-responsivity UV photodetectors are in increasing demand due to their essential roles in environmental monitoring,[1] military reconnaissance,[2,3] flame detection,[4,5] and biomedical analysis.[6,7] Wide-bandgap semiconductor materials,[8−11] including zinc oxide,[12,13] aluminum gallium nitride,[14] gallium nitride,[15,16] and silicon carbide,[17] are extensively applied in UV detection. Notably, devices made from these materials do not require a filter.[18] However, impurities and lattice defects in wide-bandgap semiconductors scatter carriers, resulting in a decrease in mobility and thereby increasing the probability of photogenerated electrons and holes recombining before reaching the electrode. Developing materials with high carrier mobility is crucial for enhancing device performance. Graphene, a representative two-dimensional carbon material, has an ultrahigh carrier mobility of 15,000 $cm^2/(V \cdot s)$.[19,20] Yet, its monolayer structure leads to low light absorption, which restricts its UV response. The SiC[21] has a wide bandgap, which can effectively absorb ultraviolet light. Constructing a Gr/SiC heterojunction synergizes their advantages, coupling graphene's fast carrier transport with silicon carbide's strong UV absorption to enhance device optoelectronic performance.[22] Extensive research on Gr/SiC photodetectors, current efforts mainly focus on modifying graphene through nanoparticles, electrical doping, and chemical doping.

Nanoparticle modification[23] of graphene is a key approach to improve optoelectronic performance of the Gr/SiC device by primarily leveraging the surface plasmon resonance effect of the nanoparticle to enhance UV light absorption. Khadk et al.[23] utilized surface plasmon resonance effect of gold nanoparticles to fabricate ultralow power photodetectors, increasing light absorption to enhance responsivity. Under a bias voltage of −0.01 V, the device exhibited a responsivity of 2 × 10^{-2} A/W for 365 nm ultraviolet light, a normalized detectivity of 3 × 10^6 Jones. Nevertheless, this technique encounters significant practical challenges. First, nanoparticles introduced onto graphene create additional scattering centers, impeding efficient carrier transport and reducing carrier mobility substantially. Second, the weak adhesion between nanoparticles and the graphene makes nanoparticles prone to aggregation and detachment during long-term operation, undermining device stability and shortening its lifespan.

The electrical doping[24] of graphene is also an important means to optimize the performance of Gr/SiC devices. By

Received: April 25, 2025
Revised: July 27, 2025
Accepted: July 27, 2025
Published: August 4, 2025

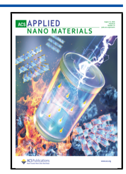

https://doi.org/10.1021/acsanm.5c02220
ACS Appl. Nano Mater. 2025, 8, 15799–15807

applying a gate voltage, the Fermi level of graphene can be effectively tuned, substantially increasing the carrier concentration and enhancing the carrier transport efficiency. Li et al.[25] achieved a responsivity of 103.3 A/W for 261 nm ultraviolet light through gate voltage modulation in NiO/Gr/4H-SiC structures under 5 V source-drain voltage and −3 V gate voltage. In further studies,[24] their optimized Gr/4H-SiC device reached a responsivity of 254.1 A/W for 325 nm light. However, practical implementation of the doping technique has many limitations. For example, the effect of electrical doping primarily depends on the characteristics of the gate dielectric material. A mismatch between the gate dielectric material's work function and the Gr/SiC system can lead to issues such as low charge injection efficiency or excessive interface charge accumulation.[26] In addition. upon carrier injection via electrical doping, these carriers interact with material atoms, which disrupts the continuous energy band structure, giving rise to localized energy levels or impurity energy levels. These additional energy levels act as carrier traps to randomly capture photogenerated carriers during transport, significantly reducing the number of effective carriers contributing to photocurrent.[27]

Chemical doping[28] of graphene in Gr/SiC devices can increase carrier concentration by introducing impurity atoms that provide extra electrons or holes. Henck et al.[29] designed an n-MoS_2/p-bilayer graphene heterojunction to enable tunable photoresponse, achieving a responsivity of 1.4×10^{-2} A/W at 1 V bias. However, strongly oxidizing or reducing dopants may corrode the graphene surface, inducing crystal lattice distortion and chemical bond cleavage. These alterations disrupt carrier transport pathways, thereby significantly diminishing the carrier mobility. Simultaneously, defect states generated during doping act as recombination centers for photogenerated carriers, drastically shortening their lifetimes. Moreover, these defects will form active sites, which will promote the occurrence of chemical reactions between graphene and substances such as oxygen and moisture in the environment, significantly reducing its chemical stability and physical properties.[30]

Compared to nanoparticle modification, electrical doping, and chemical doping of graphene, the regulation of graphene's own quality offers the advantage of a simpler process. This feature renders it highly promising for industrial production, as it better aligns with the demands for efficient and convenient manufacturing processes. The goal of this work is to obtain a high-responsivity device with high repeatability, reliable performance, and low cost with a simple fabrication procedure.

Herein, pyrolytic epitaxy on SiC substrates was employed to prepare the Gr/SiC heterojunction samples with various qualities under different temperature and growth time conditions, which were then used to fabricate the Gr/SiC heterojunction devices. In this device, SiC serves as the absorption layer and graphene serves as the transport layer. The holes generated by photoexcitation in SiC are injected into the conduction band of graphene, while the electrons remain in SiC. The high carrier mobility of single-layer graphene enables the photogenerated carriers to rapidly migrate to the electrodes, further reducing carrier recombination and increasing the responsivity. The device's optoelectronic performance was systematically characterized by measuring its current−voltage ($I-V$) characteristics, responsivity−voltage ($R-V$) curves, responsivity−incident light power ($R-P$) relationships, and spectral responsivity. Specifically, a fully covered monolayer graphene with an area of 3.5×4.5 mm^2 was grown on SiC at 1640 °C for 1400 s, which possesses the highest mobility of 3020.54 $cm^2/(V \cdot s)$ among all samples. The device fabricated from this sample exhibited outstanding optoelectronic performance. Under 275 nm UV irradiation with a power of 0.004 μW, it achieved a remarkable responsivity of 5425 A/W, a photoconductive gain of 24462, and a normalized detectivity of 1.10×10^{13} Jones. Moreover, the photoresponse mechanism of the detector is analyzed based on the device's energy band diagram.

■ RESULTS AND DISCUSSION

Graphene is grown by SiC epitaxy, and UV photodetectors are fabricated using photolithography and reactive ion etching (RIE) technologies. The fabrication process and device structure are listed in Figure 1. The device, has a planar structure of metal−graphene-metal configuration, in which there are vertical Gr/SiC heterojunctions. The Gr/SiC heterojunctions functions as the light-absorbing layer, and meanwhile, graphene also serves as the carrier transport layer. The results of UV−vis absorption spectroscopic characterization show that the light absorptivity of Gr/SiC is improved by about 10% over pure SiC in the wavelength range from 200 to 800 nm and the optical band gap of SiC is 3.16 eV corresponding to the absorption cutoff wavelength of 392.4 nm (see Figure S1). When no external bias is applied, the photocurrent (I_{ph}) of the detector under UV light is almost zero (see Figure S2), indicating that the detector must operate in photoconductive mode.[31]

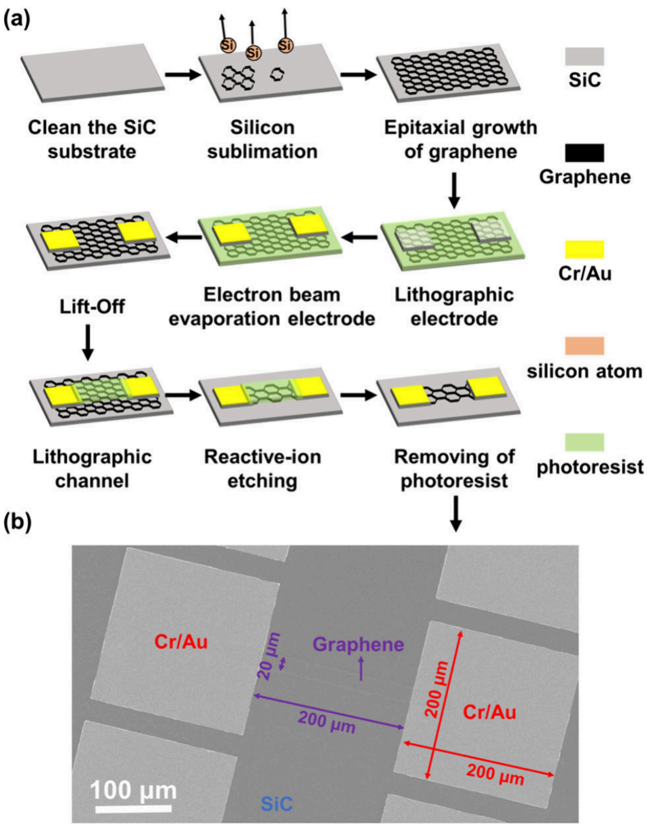

Figure 1. (a) Process flow of device preparation and (b) SEM image of the UV photodetector.

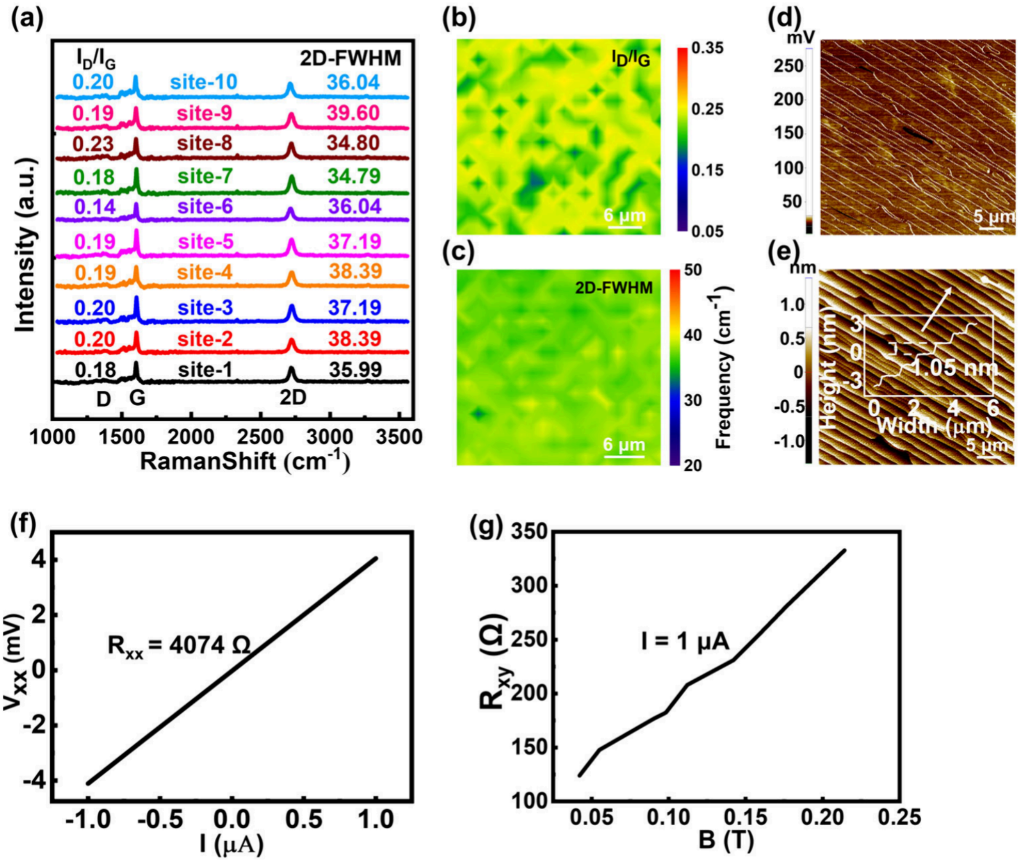

Figure 2. Characterization of the best quality graphene grown at 1640 °C for 1400 s. (a) Raman spectra collected from ten discrete positions on the graphene. (b) Raman mapping measurement of the ratio of the intensities of peak D to peak G (I_D/I_G). (c) Raman mapping measurement of the fwhm of the 2D peak. (d) Lateral force microscopy (LFM) image of graphene epitaxially grown on SiC and (e) height topography of (d). The inset shows the height profile along the arrow direction. (f) *Vxx*−*I* relationship diagram. (g) *Rxy*−*B* relationship diagram. The test was carried out at room temperature and atmospheric pressure with a constant current $I = 1\ \mu$A.

The photoelectric performance of the device is closely related to the dimensions of the graphene channel. To investigate this relationship, photodetectors with varying graphene channel sizes were fabricated and characterized (Figure S3). Among them, devices with a graphene channel size of 200 μm × 20 μm demonstrated the best optoelectronic performance. Hence, this optimal channel size was chosen for subsequent testing and analysis.

The quality of graphene significantly limits the optoelectronic performance of the device.[32] In this study, graphene samples of varying quality were prepared under different temperature (Figures S4 and S5) and growth time (Figures S6 and S7) conditions. The full width at half-maximum of the 2D peak (2D-fwhm) of the Raman spectra of various quality graphene is summarized in Table S1. Analysis of the 2D-fwhm data reveals that, at a fixed growth time of 1400 s, monolayer graphene (2D-fwhm < 40 cm^{-1}) can be grown at 1540−1640 °C. When the growth temperature is set at 1640 °C, samples grown for 1100−1400 s are all monolayer graphene. Lateral force microscopy (LFM) images show that at the same growth time of 1400 s, lower temperatures (1540 or 1590 °C) result in more ungrown SiC regions and defects (see white irregular areas in Figure S5). When the growth time is shortened to 1100 s at the same growth temperature of 1640 °C, a buffer layer that has not been completely converted into graphene forms on the surface of the sample, which is manifested as white stripes perpendicular to the steps in Figure S7. Ultimately, the optimal conditions for growing large-area monolayer graphene are a temperature of 1640 °C and a time of 1400 s.

We further characterized the structure and electrical properties of graphene grown under optimal conditions. Raman spectra collected from ten discrete positions on the sample show three characteristic peaks at 1350 cm^{-1} (D peak), 1580 cm^{-1} (G peak), and 2700 cm^{-1} (2D peak),[33,34] which confirm the successful growth of graphene on the SiC substrate[24] (see Figure 2a). In addition, the Figure 2a indicates an average I_D/I_G ratio of around 0.19 revealing few defects in the graphene, and a 2D-fwhm of approximately 36.84 cm^{-1} confirming the monolayer structure of graphene.[35,36] Furthermore, Raman mapping over a 30 μm × 30 μm area shows an I_D/I_G ratio of 0.15−0.25 (see Figure 2b) and a 2D-fwhm of 30−40 cm^{-1} (see Figure 2c), which verify large-area monolayer graphene with a few defects. The continuous and uniform brown regions in the LFM image (Figure 2d) show that graphene fully covers the SiC substrate. As shown in Figure 2e, the height map reveals that the step height of graphene is approximately 1 nm. These results collectively confirm that large-area, single-layer, and low-defect graphene[37−39] has been successfully grown on the SiC substrate with an area of 3.5 × 4.5 mm^2. The carrier mobility of the graphene was determined by using a Hall bar structure, as illustrated in Figure S8. Figure 2f is a V_{xx}−I curve, where V_{xx} represents the voltage in the direction from position 1 to position 2 in Figure S8. The slope

https://doi.org/10.1021/acsanm.5c02220
ACS Appl. Nano Mater. 2025, 8, 15799−15807

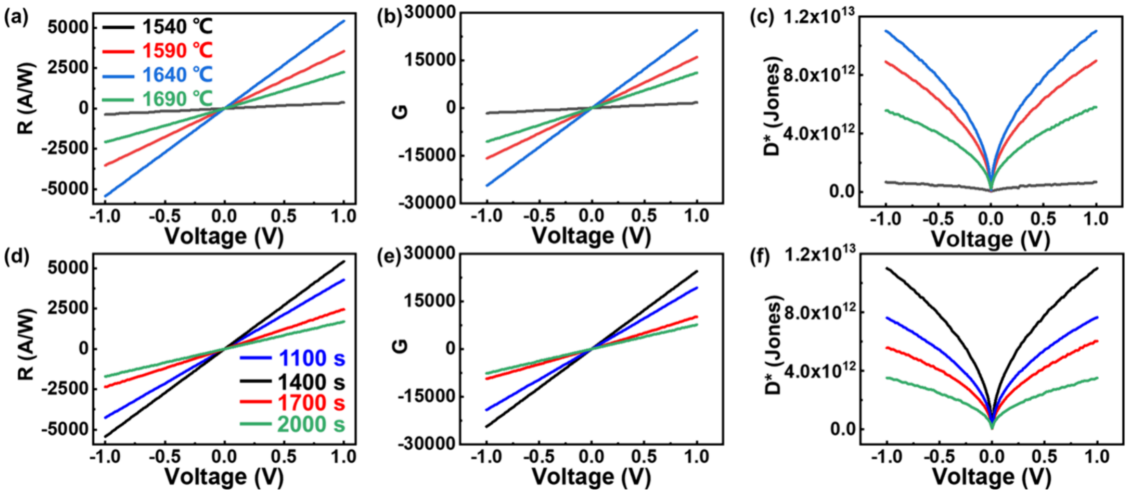

Figure 3. Optoelectronic performance of devices fabricated with graphene of different qualities under 275 nm UV irradiation at 0.004 μW: (a) R−V characteristics, (b) G−V characteristics, (c) D^*−V characteristics for graphene grown at different temperatures with a 1400 s duration. (d) R−V characteristics, (e) G−V characteristics, and (f) D^*−V characteristics for graphene grown at 1640 °C for different durations.

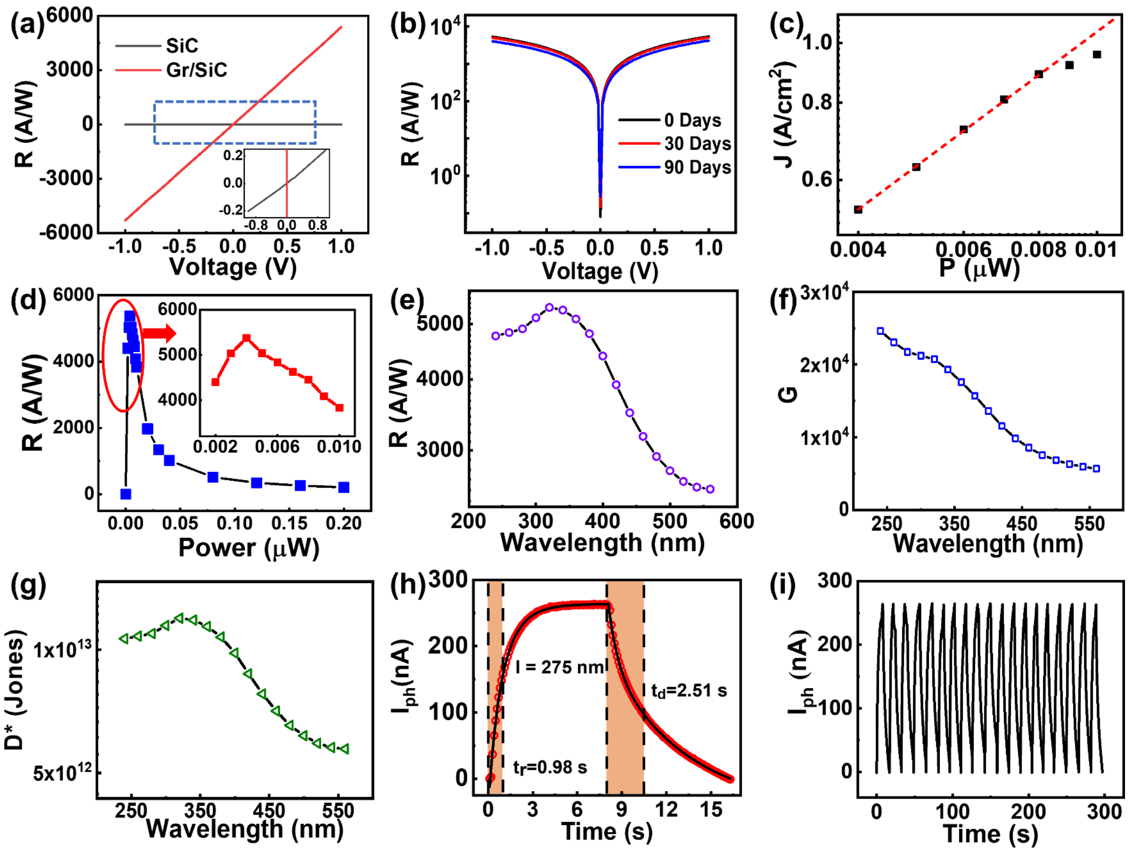

Figure 4. Photoelectric performance of the optimal detector under UV irradiation of 0.004 μW at 275 nm. (a) Comparison of the responsivity of detectors with and without graphene The illustration is an enlarged view of the area within the rectangular blue frame. (b) The curve of responsivity versus bias voltage for the device tested for 0 day and after being stored in air for 30 and 90 days. (c) The relationship between photocurrent density (J) and optical power. (d) R−P relationship diagram under the UV radiation at 275 nm and a bias voltage of 1 V. Inset: the enlarged view of the area within the red elliptical frame. (e) R−λ, (f) G−λ and (g) D^*−λ relationship diagram under UV irradiation of 0.003 μW. (h) Time-resolved photoresponses of the detector at a bias voltage of 0.01 V. (i) Time-resolved photo response of the device under multiple cyclic on/off UV irradiation at a bias voltage of 0.01 V.

of this curve yields a graphene resistance of R_{xx} = 4074 Ω. Using Formula (4) in the Supporting Information, the resistivity ρ of the graphene was calculated to be 3760.62 Ω·cm. Figure 2g is the R_{xy}-B curve, where the R_{xy} denotes the resistance in the vertical direction from position 1 to position 3 in Figure S8 and B is the magnetic field. The slope of this curve corresponds to a Hall coefficient R_H of 1135.91 m^2/C. According to Formula (7) in the Supporting Information, the carrier mobility of the monolayer graphene grown at 1640 °C for 1400 s can be calculated, and it is as high as 3020.54

https://doi.org/10.1021/acsanm.5c02220
ACS Appl. Nano Mater. 2025, 8, 15799−15807

$cm^2/(V\cdot s)$. Compared with the highest mobility of graphene in previously fabricated devices (1298.38 $cm^2/(V\cdot s)$),[24] this mobility value has increased to 2.3 times.

To evaluate the performance of the detector, several key indicators are calculated as follows. The responsivity (R) is a key indicator for evaluating the performance of photodetectors. According to formula 1, the responsivity of the device can be obtained by the ratio of photocurrent (I_{ph}) to the effective incident light power (P).[40] The I_{ph} is the difference between the current under UV irradiation (I_{light}) and the dark current (I_{dark}).[24] The P is equal to the product of the light power density (P_D) and the effective light absorption area (A) of the detector.[25] The light power density is obtained from Figure S9, and the effective light absorption area of the photoconductive detector is the channel area[41] which is 200 μm × 20 μm in this study.

$$R = \frac{I_{ph}}{P} = \frac{I_{ph}}{P_D \times A} \tag{1}$$

The high responsivity of photoconductive detectors generally originates from a large photoconductive gain G, which can be calculated according to formula 2:[24]

$$G = \frac{\tau}{\tau_t} = \frac{I_{ph}/\mathrm{e}}{P/\mathrm{h}\nu} \tag{2}$$

where τ is the carrier lifetime, τ_t is the carrier transit time, e is the electron charge, h is Planck's constant, and ν is the light frequency.

The noise equivalent power (NEP) represents the sensitivity of a detector. It is defined as the minimum incident optical power required to achieve a unitary signal-to-noise ratio over a bandwidth of 1 Hz. For a photoconductance type detector, the NEP is calculated according to Formula 3.[42]

$$\mathrm{NEP} = \frac{P}{V_S/V_N} = I_N/R = \sqrt{2eI_{dark}}/R \tag{3}$$

where V_S/V_N is the signal-to-noise ratio, I_N is the noise current spectral density.

Based on the NEP, normalized detectivity (D^*) further normalizes the effective light absorption area of the detector, which is calculated according to formula 4:[40−42]

$$D^* = \sqrt{A}/\mathrm{NEP} \tag{4}$$

The performance of the devices fabricated using different quality graphene was systematically tested (see Figure 3). The results show that under UV irradiation of 0.004 μW at 275 nm, a device fabricated from graphene grown at 1640 °C for 1400 s exhibits the optimal performance with R of 5425 A/W, G of 24462 and D^* of 1.10 × 10^{13} Jones.

For the optimal detector, we conducted further performance tests and analyses. As shown in Figure 4a, we fabricated a UV photodetector with pure SiC as the control group. The pure SiC detector exhibited an R of merely 0.24 A/W, significantly lower than that of the Gr/SiC detector. The lower electrical conductivity of SiC impeded carrier transport, consequently reducing the photocurrent. Figure 4b shows that R rises with increasing bias voltage. Higher bias voltages strengthen the interelectrode electric field, accelerating carrier drift and reducing recombination, allowing more photogenerated carriers to reach the electrodes and enhancing photocurrent. Moreover, after 30 and 90 days of air exposure, R values remain stable compared to the initial measurements, indicating consistent photoelectric performance.

Figure 4c demonstrates that photocurrent densities exhibit an approximately linear relationship with optical power within a certain range. At low optical powers, the yield of photocarriers is proportional to the number of incident photons: more photons imply the more electron−hole pairs, thereby forming a larger photocurrent. However, as the optical power increases, the photocurrent will saturate eventually. This is attributed to balance due to the rapidly increased hole−electron recombination with the increase hole−electron pair density.

Figure 4d reveals that R initially rises and then declines as the P increases, and the R reaches its peak value under UV light with a power of 0.004 μW at 275 nm. At low power, limited carrier generation allows a near-complete collection to form a photocurrent. Conversely, high power triggers a surge in carrier production, causing recombination within the detector. This recombination effect will cause the growth rate of the photocurrent to be lower than that of the optical power.[43] The results highlight its suitability for low-light detection applications, particularly at the nanowatt power level.[44] Furthermore, the G and D^* of the detector were characterized and the results are shown in Figure S10 for different bias voltages and Figure S11 for different P values. It shows that G and D^* reach their maximum values under UV irradiation of 0.004 μW at 275 nm and a bias voltage of 1 V. Figure 4e-g illustrates the dependence of R, G and D^* on the wavelength of the incident light. Both R and D^* initially rises and then declines as the wavelength increases, while the G declines as the wavelength increases. In the 240−400 nm UV range, both R, G and the D^* remain above 4395.3 A/W, 13625 and 9.81 × 10^{12} Jones, respectively. Beyond this spectral range, R, G and D^* drop sharply. The above results indicate that the detector is highly sensitive to light with wavelengths ranging from 240 to 400 nm and is an excellent UV detector. The UV−vis absorption spectrum in Figure S1 indicates that the absorption cutoff wavelength of the SiC is 392.4 nm. Wavelengths longer than this value led to reduced absorption and thus subsequent optoelectronic performance degradation.

The rise time and fall time are used to evaluate the response speed of the detector, and they were determined by testing time-resolved photoresponses, as shown in Figure 4h. The rise time refers to the time required for the photocurrent signal to rise from 0 to 1−1/e (i.e., 63.2%) of the peak, and the fall time is the time required for the photocurrent signal to fall from the peak to 1/e (i.e., 36.8%) of the peak.[45] At a bias voltage of 0.01 V, the device exhibited a rise time of 0.98 s and a fall time of 2.51 s. Compared to other devices, its relatively slow response is attributed to the complex carrier exchange between graphene and SiC.[22] The movement speed of photogenerated carriers from the SiC to the Gr/SiC interface is reduced through lattice vibration and impurity scattering. Moreover, defects and impurity energy levels in the materials act as trap states to capture photogenerated electrons or holes, which leads to the carriers returning to the conduction process only after lingering in these trap states for a specific duration. These prolongs their effective transport time, resulting in a slower response speed. Figure 4i shows dynamic photo response after 19 cycles of UV on/off irradiation, confirming the reproducibility of the device's photoresponse. From Figure 4i, the calculated mean value of the photocurrent peak for each cycle is 263.95 nA with

https://doi.org/10.1021/acsanm.5c02220
ACS Appl. Nano Mater. 2025, 8, 15799−15807

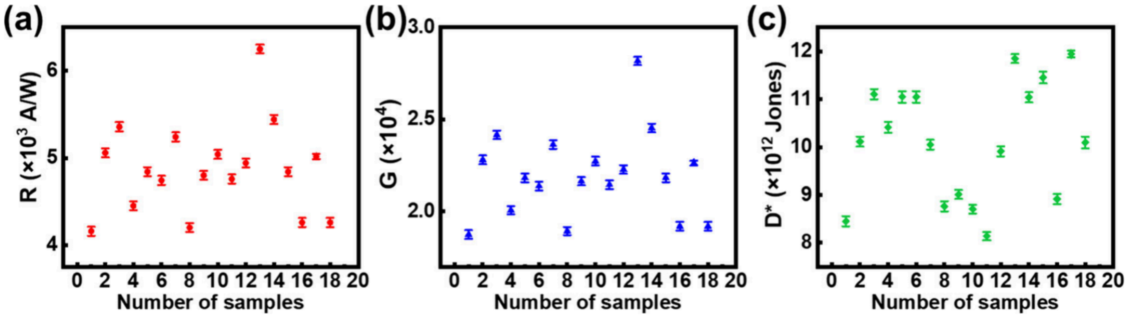

Figure 5. Performance of the 18 detectors under UV irradiation of 0.004 μW with a wavelength of 275 nm and a bias voltage of 1 V. (a) R (b) G and (c) D^*.

Table 1. Comparison of Gr/SiC-Based UV Photodetectors

Materials	λ (nm)	Bias voltage (V)	R (A/W)	G	D^* (Jones)
Gr/MoS_2/SiC[29]	405	1	0.014	0.043	–
ITO/Gr/SiC[46]	325	0.3	0.0117	–	–
EG/SiC[47]	270	20	17	–	4.4×10^{13}
Gr/h-BN/SiC[48]	185	0	0.015	0.10	–
Gr/ZnS QDs/SiC[49]	250	0	2.9×10^{-4}	0.0136	–
Gr/γ-Ga_2O_3NDs/SiC[50]	250	0	5.8×10^{-3}	–	7.6×10^{10}
Gr/SiC/Gr[51]	325	–	2.38×10^{-4}	–	1.3×10^{14}
Gr/4H-SiC[24]	325	−3	254.1	–	–
Gr/AlGaN/SiC[28]	265	0	0.081	0.381	–
NiO/Gr/SiC[25]	261	5	103.3	490.80	1.07×10^{13}
AuNPs/QFSG/SiC[23]	365	−0.01	0.02	–	3×10^{6}
Gr/SiC[52]	280	30	1.17	51800	3.14×10^{14}
Gr/SiC NW array[53]	275	5	2.59	888130	–
β-Ga_2O3/Gr/SiC[54]	255	−1	0.074	–	5×10^{12}
Gr/SiC-This Work	**275**	**1**	**5425**	**24462**	$\mathbf{1.10 \times 10^{13}}$

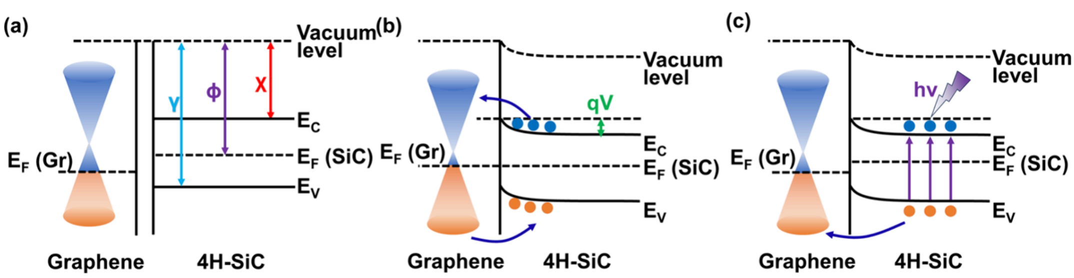

Figure 6. Energy band diagrams of Gr/SiC heterojunctions. (a) Before reaching equilibrium and after reaching equilibrium (b) without and (c) with UV irradiation. The incident UV photon energy is expressed as hν.

a standard deviation of 0.62. This indicates excellent cyclic stability for the same device.

To assess the fluctuations in the performance of photodetectors, the performances of an array of 18 photodetectors with identical dimensions were tested (see Figure 5). Under UV irradiation of 0.004 μW at 275 nm, all devices exhibited similar performance metrics: the $R \approx 5 \times 10^3$ A/W, the $G \approx 2 \times 10^4$ and the $D^* \approx 1 \times 10^{13}$ Jones. These results indicate that the preparation process exhibits excellent repeatability and there are no extreme failure cases. This fully validates the reliability of the preparation method and also preliminarily demonstrates its potential for mass production.

Table 1 summarizes the test conditions and performance of previously reported Gr/SiC-based UV photodetectors. For most of these devices, R typically ranges from 10^{-2} to 10^2 A/W, G from 10^{-1} to 10^2%, and D^* from 10^{10} to 10^{14} Jones. In contrast, our device outperforms the vast majority of these counterparts in terms of photoelectric performance.

In order to understand the reason for the high response of the UV photodetector, the energy band diagrams of the heterojunctions between graphene and SiC are illustrated in Figure 6. Notably, graphene has a Fermi level lower than that of the SiC (see Figure S12). Under UV light illumination, electron−hole pairs are mainly generated in SiC. Driven by the built-in electric field of the Gr/SiC heterojunction, the photogenerated electron−hole pairs are separated and injected onto graphene (see Figure 6c). In graphene with high mobility, the photogenerated carrier can move quickly to the electrode under the drive of an applied electric field, significantly reducing the drift time between the two electrodes and generating a huge photoconductive gain.

https://doi.org/10.1021/acsanm.5c02220
ACS Appl. Nano Mater. 2025, 8, 15799−15807

■ CONCLUSIONS

In this study, thermal decomposition epitaxy at 1640 °C for 1400 s successfully grew high-quality (μ = 3020.54 $cm^2/(V{\cdot}s)$) monolayer graphene on a 3.5 × 4.5 mm^2 SiC surface. The photodetector based on this Gr/SiC heterojunction demonstrated a remarkable responsivity of over 4000 A/W in the wavelength range from 240 to 400 nm. In particular, under UV irradiation of 0.004 μW at 275 nm, the photodetector achieved outstanding performance: R of 5425 A/W, the G of 24462, and the D^* of 1.10 × 10^{13} Jones. These metrics surpass those of most UV photodetectors based on graphene/SiC materials. The Gr/SiC detector's superior response stems from graphene's high carrier mobility, which can rapidly transport photogenerated carriers and shorten the carrier drift time, thereby significantly enhancing the photoconductive gain. Moreover, the simplified preparation process reduces costs, shortens production time, and improves mass-production viability, providing key support for the industrial application of high-responsivity UV photodetectors.

■ EXPERIMENTAL SECTION

Graphene Preparation. Graphene was prepared by using the thermal decomposition epitaxy method. A semi-insulating 4H-SiC sample (3.5 × 4.5 mm^2, 360 μm thick, purchased from Shandong Tianyue Advanced Materials Technology Co., Ltd.) was thoroughly cleaned by ultrasonic treatment in acetone, isopropyl alcohol and deionized water and placed in a graphite crucible of specific dimensions. The system was evacuated to a high-vacuum state using a mechanical pump and a molecular pump. The temperature was raised to 800 °C, and the sample was annealed for 20 min to remove water and impurities. Argon gas (500 sccm) was introduced as a carrier gas, and the temperature was increased to 1200 °C for a 20 min annealing, causing step bunching to convert small steps into larger ones. Then, the temperature was raised to approximately 1580 °C and maintained for 23 min to grow graphene. Graphene preparation as shown in Figure 1.

Gr/SiC UV Photodetector Fabrication. The device fabrication process is initiated with photoresist spin-coating onto the Gr/SiC substrate, followed by a standard photolithography procedure (exposure and development) to define electrode patterns. Graphene in the electrode regions was selectively etched using reactive ion etching (RIE) with 50 sccm O_2 at 35 W for 5 s. Then 20 nm Cr and 20 nm Au were sequentially deposited on the material to form metal contacts and electrodes after follow up metal lift off procedure. Next, graphene was patterned by the photoresist coating, exposure, and development processes. Unprotected graphene regions were etched away using RIE with mixture of 100 sccm O_2 and 300 sccm Ar gas under 30 W power for 30 s. The photoresist residue was removed by acetone cleaning. Finally, a patterned graphene UV PD array with metal leads is successfully fabricated.

Characterization. The surface morphology and thickness of graphene were examined using an atomic force microscope (Park NX10). The quality of the graphene was characterized using a Raman spectrometer (Andor Shamrock500i, Raman mapping test size: 30 μm × 30 μm, step size: 3 μm). The UV absorption of Gr/4H-SiC was characterized by using a UV–vis spectrophotometer (U-3900). The morphology and structure of the device were assessed by using a scanning electron microscope (Hitachi SU3500).

Photoelectric Performance Testing. The performance of the UV photodetector was tested in a custom-built darkroom, with the setup diagram shown in Figure S13. The darkroom contained a UV lamp (wavelength 275 nm, with adjustable light power density via an applied voltage). The spectral response was evaluated by using a monochromator (LSR-X150 xenon lamp source) and a source meter (KEITHLEY 2612B).

■ ASSOCIATED CONTENT

Data Availability Statement

The data that support the findings of this study are available from the corresponding author upon reasonable request.

Supporting Information

The Supporting Information is available free of charge at https://pubs.acs.org/doi/10.1021/acsanm.5c02220.

> Measurements for fuction difference between graphene and silicon carbide, influence of irradiating light power, bias voltage, power density on photodetectors performance, and characterization (Raman, LFM of the Prepared samples) (PDF)

■ AUTHOR INFORMATION

Corresponding Authors

Yanqing Ma − *Tianjin International Center for Nanoparticles and Nanosystems, Tianjin University, Tianjin 300072, China; Tianjin Key Laboratory for Low-dimensional Electronic Materials and Advanced Instrumentation, Tianjin 300072, China; School of Precision Instrument and Optoelectronics Engineering, Tianjin University, Tianjin 300072, China; Haihe Laboratory for Low-dimensional Electronic Materials, Tianjin 300074, P.R. China;* orcid.org/0000-0002-3317-8273; Email: mayanqing@tju.edu.cn

Lei Ma − *Tianjin International Center for Nanoparticles and Nanosystems, Tianjin University, Tianjin 300072, China; Tianjin Key Laboratory for Low-dimensional Electronic Materials and Advanced Instrumentation, Tianjin 300072, China; Haihe Laboratory for Low-dimensional Electronic Materials, Tianjin 300074, P.R. China;* orcid.org/0000-0002-2446-4833; Email: lei.ma@tju.edu.cn

Authors

Xue Wang − *Tianjin International Center for Nanoparticles and Nanosystems, Tianjin University, Tianjin 300072, China*

Cao Tang − *Tianjin International Center for Nanoparticles and Nanosystems, Tianjin University, Tianjin 300072, China*

Rui Li − *Tianjin International Center for Nanoparticles and Nanosystems, Tianjin University, Tianjin 300072, China*

Xiaodong Zhu − *Tianjin International Center for Nanoparticles and Nanosystems, Tianjin University, Tianjin 300072, China; Haihe Laboratory for Low-dimensional Electronic Materials, Tianjin 300074, P.R. China*

Wei Jin − *Tianjin International Center for Nanoparticles and Nanosystems, Tianjin University, Tianjin 300072, China*

Luzhen Hao − *Tianjin International Center for Nanoparticles and Nanosystems, Tianjin University, Tianjin 300072, China*

Rongke Sun − *Tianjin International Center for Nanoparticles and Nanosystems, Tianjin University, Tianjin 300072, China*

Jinwei Liu − *Tianjin International Center for Nanoparticles and Nanosystems, Tianjin University, Tianjin 300072, China*

Complete contact information is available at: https://pubs.acs.org/10.1021/acsanm.5c02220

Author Contributions

Xue Wang: Methodology, Investigation, Data curation, original draft preparation. **Cao Tang:** Completed the investigation and data curation. **Rui Li:** Performed photolithography experiments. **Xiaodong Zhu, Wei Jin, Luzhen Hao, Rongke Sun, Jinwei Liu:** Analyzed the data and discussed the results. **Yanqing Ma:** Writing-review and editing, Supervision. **Lei Ma:** Conceptualization, Supervision, Methodology, Validation, Writing-review and editing.

Notes

The authors declare no competing financial interest.

■ ACKNOWLEDGMENTS

This work was financially supported by the National Key R&D Program of China (No. 2022YFC3006303).

■ REFERENCES

(1) Spangenberg, M.; Bryant, J. I.; Gibson, S. J.; Mousley, P. J.; Ramachers, Y.; Bell, G. R. Ultraviolet Absorption of Contaminants in Water. *Sci. Rep.* **2021**, *11* (1), 3682.

(2) Pandit, B.; Schubert, E. F.; Cho, J. Dual-Functional Ultraviolet Photodetector with Graphene Electrodes on AlGaN/GaN Heterostructure. *Sci. Rep.* **2020**, *10* (1), 22059.

(3) Rogalski, A.; Bielecki, Z.; Mikolajczyk, J.; Wojtas, J. Ultraviolet Photodetectors: From Photocathodes to Low-Dimensional Solids. *Sensors* **2023**, *23* (9), 4452.

(4) Tan, Y. M.; Mu, G.; Rao, T. Y.; Luo, Y. N.; Zhao, P. F.; Chen, M. L.; Tang, X. Perovskite Colloidal Quantum-Dot Enhanced Graphene/Silicon Heterojunction with Improved Ultraviolet Response. *Appl. Phys. Lett.* **2023**, *122* (5), 051102.

(5) Yadav, P.V. K.; Ajitha, B.; Kumar Reddy, Y. A.; Sreedhar, A. Recent Advances in Development of Nanostructured Photodetectors from Ultraviolet to Infrared Region: A Review. *Chemosphere* **2021**, *279*, 130473.

(6) Aboamer, M. A.; Elgohary, D. H.; Almukil, A. A.; Aboamer, A. A.; Alarifi, I. M.; Bakouri, M.; Rahman Mohamed, N. A. A Comparative Study of Mechanical Behavior of ABS Material Based on UVC Sterilization for Medical Usage. *J. Mech. Sci. Technol.* **2022**, *36* (7), 3373.

(7) Dousset, L.; Poizeau, F.; Robert, C.; Mansard, S.; Mortier, L.; Caumont, C.; Routier, É.; Dupuy, A.; Rouanet, J.; Battistella, M.; Greliak, A.; Cappellen, D.; Galibert, M. D.; Allayous, C.; Lespagnol, A.; Gerard, É.; Kerneuzet, I.; Roy, S.; Dutriaux, C.; Merlio, J. P.; Vergier, B.; Schrock, A. B.; Lee, J.; Ali, S. M.; Kammerer-Jacquet, S. F.; Lebbé, C.; Beylot-Barry, M.; Boussemart, L. Positive Association between Location of Melanoma, Ultraviolet Signature, Tumor Mutational Burden, and Response to Anti-PD-1 Therapy. *Jco Precis Oncol* **2021**, *5*, 1821.

(8) Li, X. S.; Liu, X.; Li, Y. D.; Gao, D. H.; Cao, L. Z. Using Novel Semiconductor Features to Construct Advanced ZnO Nanowires-Based Ultraviolet Photodetectors: A Brief Review. *IEEE Access* **2021**, *9*, 11954.

(9) Kumar, A.; Khan, M. A.; Kumar, M. Recent Advances in UV Photodetectors Based on 2D Materials: A Review. *J. Phys. D: Appl. Phys.* **2022**, *55* (13), 133002.

(10) Gupta, P. K.; Pandey, U.; Pal, B. N.; Pandey, A. Low-Cost Solution-Processed MoS_2 Quantum Dots-Based Deep UV Photodetector for Monitoring Disinfection. *IEEE Trans. Electron Devices* **2022**, *69* (5), 2474.

(11) Wang, J.; Xing, Y.; Wan, F.; Fu, C.; Xu, C. H.; Liang, F. X.; Luo, L. B. Progress in Ultraviolet Photodetectors Based on II-VI Group Compound Semiconductors. *J. Mater.* **2022**, *10* (36), 12929.

(12) Jehad, A. K.; Fidan, M.; Ünverdi, Ö.; Çelebi, C. CVD Graphene/SiC UV Photodetector with Enhanced Spectral Responsivity and Response Speed. *Sensor Actuat A-Phys.* **2023**, *355*, 114309.

(13) Peng, Y. Y.; Jiang, D. Y.; Zhao, M.; Duan, Y. H.; Wei, H. M.; Li, H. D.; Liang, Q. C.; Wang, S. W. High-Performance UV-Visible Photodetectors Based on ZnO/Perovskite Heterostructures. *J. Alloys Compd.* **2023**, *965*, 171372.

(14) Chen, Y. R.; Shi, J. W.; Zhang, Z. W.; Miao, G. Q.; Jiang, H.; Song, H. AlGaN-Based Solar-Blind UV Heterojunction Bipolar Phototransistors: Structural Design, Epitaxial Growth, and Optoelectric Properties. *J. Mater.* **2023**, *11* (23), 7697.

(15) Ma, Y.; Zhao, X.; Chen, H.; Wei, W.; Shen, L. Progress and Perspective of Perovskite Thin Single Crystal Photodetectors. *Acta Phys. Chim. Sin* **2025**, *41* (4), 100030.

(16) Han, Y. R.; Wang, Y. F.; Fu, S. H.; Ma, J. A.; Xu, H. Y.; Li, B. S.; Liu, Y. C. Ultrahigh Detectivity Broad Spectrum UV Photodetector with Rapid Response Speed Based on p-β Ga_2O_3/n-GaN Heterojunction Fabricated by a Reversed Substitution Doping Method. *Small* **2023**, *19* (16), 2206664.

(17) Aslanidou, S.; García-García, A.; Godignon, P.; Rius, G. Electronic Interface and Charge Carrier Density in Epitaxial Graphene on Silicon Carbide. A Review on Metal-Graphene Contacts and Electrical Gating. *APL Mater.* **2020**, *8* (10), 100702.

(18) Chen, J. X.; Ouyang, W. X.; Yang, W.; He, J. H.; Fang, X. S. Recent Progress of Heterojunction Ultraviolet Photodetectors: Materials, Integrations, and Applications. *Adv. Funct* **2020**, *30* (16), 1909909.

(19) Winzer, T.; Knorr, A.; Malic, E. Carrier Multiplication in Graphene. *Nano Lett.* **2010**, *10* (12), 4839.

(20) Wu, X. S.; Hu, Y. K.; Ruan, M.; Madiomanana, N. K.; Hankinson, J.; Sprinkle, M.; Berger, C.; de Heer, W. A. Half Integer Quantum Hall Effect in High Mobility Single Layer Epitaxial Graphene. *Appl. Phys. Lett.* **2009**, *95* (22), 223108.

(21) Bhatnagar, M.; Baliga, B. J. Comparison of 6H-SiC, 3C-SiC, and Si for Power Devices. *IEEE Trans. Electron Devices* **1993**, *40* (3), 645.

(22) Lin, F.; Chen, S. W.; Meng, J.; Tse, G.; Fu, X. W.; Xu, F. J.; Shen, B.; Liao, Z. M.; Yu, D. P. Graphene/GaN Diodes for Ultraviolet and Visible Photodetectors. *Appl. Phys. Lett.* **2014**, *105* (7), 073103.

(23) Khadka, I.B.; Alluri, N.R.; Alsardia, M.M.; Joseph Raj, N.P.M.; Prasanna, A.P.S.; Ul Haq, B.; Kim, S.J.; Kim, S.-H. Ultra-Low-Power Photodetector Based on a High-Photoresponse, Plasmonic-Effect-Induced Gateless Quasi-Freestanding Graphene Device. *Appl. Surf. Sci.* **2023**, *610*, 155275.

(24) Li, Y. M.; Chen, P.; Chen, X. F.; Xu, R.; Liu, M. H.; Zhou, J.; Ge, C.; Peng, H. C.; Mao, X. K.; Feng, J. B.; Hu, X. B.; Peng, Y.; Xu, X. G.; Xie, Z. L.; Xiu, X. Q.; Chen, D. J.; Liu, B.; Han, P.; Shi, Y.; Zhang, R.; Zheng, Y. D. High-Responsivity Graphene/4H-SiC Ultraviolet Photodetector Based on a Planar Junction Formed by the Dual Modulation of Electric and Light Fields. *Adv. Opt. Mater.* **2020**, *8* (19), 2000559.

(25) Li, Y. M.; Chen, P.; Chen, X. F.; Gong, H. H.; Hu, X. B.; Peng, Y.; Xu, X. G.; Xie, Z. L.; Xiu, X. Q.; Chen, D. J.; Ye, J. D.; Han, P.; Shi, Y.; Zhang, R.; Zheng, Y. D. Gate-Controlled NiO/Graphene/4H-SiC Double Schottky Barrier Heterojunction Based on a Metal-Oxide-Semiconductor Structure for Dual-Mode and Wide Range Ultraviolet Detection. *ACS Appl. Electron* **2022**, *4* (4), 1807.

(26) Konar, A.; Fang, T. A.; Jena, D. Effect of High-K Gate Dielectrics on Charge Transport in Graphene-Based Field Effect Transistors. *Phys. Rev. B* **2010**, *82* (11), 115452.

(27) Kuik, M.; Koster, L. J. A.; Wetzelaer, G. A. H.; Blom, P. W. M. Trap-Assisted Recombination in Disordered Organic Semiconductors. *Phys. Rev. Lett.* **2011**, *107* (25), 256805.

(28) Li, T. T.; Zhu, S. Q.; Jia, L. M.; Lin, R. C.; Zheng, W.; Huang, F. Ultrahigh EQE (38.1%) Deep-UV Photodiode with Chemically-Doped Graphene as Hole Transport Layer. *Adv. Opt. Mater.* **2022**, *10* (5), 2102329.

(29) Henck, H.; Pierucci, D.; Chaste, J.; Naylor, C. H.; Avila, J.; Balan, A.; Silly, M. G.; Asensio, M. C.; Sirotti, F.; Johnson, A. T. C.; Lhuillier, E.; Ouerghi, A. Electrolytic Phototransistor Based on Graphene-MoS_2 Van Der Waals P-N Heterojunction with Tunable Photoresponse. *Appl. Phys. Lett.* **2016**, *109* (11), 113103.

(30) Bhatt, M. D.; Kim, H.; Kim, G. Various Defects in Graphene: A Review. *Rsc Advances* **2022**, *12* (33), 21520.

(31) Manis-Levy, H.; Shikler, R.; Golan, Y.; Sarusi, G. High Photoconductive Gain in a GaAs/Pbs Heterojunction Based SWIR Detector. *Appl. Phys. Lett.* **2020**, *117* (8), 081107.

(32) Lavin-Lopez, M. P.; Valverde, J. L.; Cuevas, M. C.; Garrido, A.; Sanchez-Silva, L.; Martinez, P.; Romero-Izquierdo, A. Synthesis and

https://doi.org/10.1021/acsanm.5c02220
ACS Appl. Nano Mater. 2025, 8, 15799−15807

Characterization of Graphene: Influence of Synthesis Variables. *Phys. Chem. Chem. Phys.* **2014**, *16* (7), 2962.
(33) Sun, C. Z.; Cai, W. W.; Hong, R. D.; Wu, J. K.; Chen, X. P.; Cai, J. F.; Zhang, F.; Wu, Z. Y. Tuning Electronic Properties of Epitaxial Multilayer-Graphene/4H-SiC (0001) by Joule Heating Decomposition in Hydrogen. *J. Phys. Chem. Solids* **2020**, *137*, 109224.
(34) Sharifi, M.; Naderi, N.; Fallahazad, P.; Eshraghi, M. J. Role of Graphene on the Optoelectrical Stability of Photodetectors Based on Porous Silicon. *Sens. Actuator A Phys.* **2020**, *310*, 112065.
(35) Ferrari, A. C.; Meyer, J. C.; Scardaci, V.; Casiraghi, C.; Lazzeri, M.; Mauri, F.; Piscanec, S.; Jiang, D.; Novoselov, K. S.; Roth, S.; Geim, A. K. Raman Spectrum of Graphene and Graphene Layers. *Phys. Rev. Lett.* **2006**, *97* (18), 187401.
(36) Wu, W. Y.; Liu, M. J.; Gu, Y.; Guo, B.; Ma, H. X.; Wang, P.; Wang, X. Y.; Zhang, R. J. Fast Chemical Exfoliation of Graphite to Few-Layer Graphene with High Quality and Large Size Via a Two-Step Microwave-Assisted Process. *Chem. Eng. J.* **2020**, *381*, 122592.
(37) Novoselov, K. S.; Geim, A. K.; Morozov, S. V.; Jiang, D.; Zhang, Y.; Dubonos, S. V.; Grigorieva, I. V.; Firsov, A. A. Electric Field Effect in Atomically Thin Carbon Films. *Science* **2004**, *306* (5696), 666.
(38) Sidorov, A. N.; Yazdanpanah, M. M.; Jalilian, R.; Ouseph, P. J.; Cohn, R. W.; Sumanasekera, G. U. Electrostatic Deposition of Graphene. *J. Nanotechnol* **2007**, *18* (13), 135301.
(39) Bae, S.; Kim, H.; Lee, Y.; Xu, X.; Park, J.-S.; Zheng, Y.; Balakrishnan, J.; Lei, T.; Ri Kim, H.; Song, Y. I.; Kim, Y.-J.; Kim, K. S.; Ozyilmaz, B.; Ahn, J.-H.; Hong, B. H.; Iijima, S. Roll-to-Roll Production of 30-Inch Graphene Films for Transparent Electrodes. *Nat. Nanotechnol* **2010**, *5* (8), 574.
(40) Yang, Y.; Liu, J. J.; Zhao, C. Y.; Liang, Q. R.; Dong, W. K.; Shi, J.; Wang, P.; Kong, D. A.; Lv, L.; Jia, L.; Wang, D. A.; Huang, C.; Zheng, S. J.; Wang, M. L.; Liu, F. C.; Yu, P.; Qiao, J. S.; Ji, W.; Zhou, J. D. A Universal Strategy for Synthesis of 2D Ternary Transition Metal Phosphorous Chalcogenides. *Adv. Mater.* **2024**, *36*, 2307237.
(41) Wang, F.; Zhang, T.; Xie, R. Z.; Wang, Z.; Hu, W. D. How to Characterize Figures of Merit of Two-Dimensional Photodetectors. *Nat. Commun.* **2023**, *14* (1), 2224.
(42) Fang, Y. J.; Huang, J. S. Resolving Weak Light of Sub-Picowatt Per Square Centimeter by Hybrid Perovskite Photodetectors Enabled by Noise Reduction. *Adv. Mater.* **2015**, *27* (17), 2804.
(43) Huang, J.; Guo, L. W.; Lu, W.; Zhang, Y. H.; Shi, Z.; Jia, Y. P.; Li, Z. L.; Yang, J. W.; Chen, H. X.; Mei, Z. X.; Chen, X. L. A Self-Powered Sensitive Ultraviolet Photodetector Based on Epitaxial Graphene on Silicon Carbide. *Chin. Phys. B* **2016**, *25* (6), 067205.
(44) Kang, T. T.; Zhang, Y. H.; Chen, P. P.; Wang, Z. H.; Yamamoto, A. Photoconductivity of InN Grown by MOVPE: Low Temperature and Weak Light Illumination. *Appl. Phys. Lett.* **2017**, *110* (4), 042104.
(45) Tanaka, Y.; Katayama, M.; Hashimoto, Y.; Sakuta, T. Measurement of Dynamic Response Time in Pulse Modulated Thermal Plasma. *Trans. Mater. Res. Soc. Jpn.* **2000**, *25* (1), 293.
(46) Yang, J. W.; Guo, L. W.; Huang, J.; Mao, Q.; Guo, Y. L.; Jia, Y. P.; Peng, T. H.; Chen, X. L. Rectified Photocurrent in a Planar ITO/graphene/ITO Photodetector on SiC by Local Irradiation of Ultraviolet Light. *J. Phys. D: Appl. Phys.* **2017**, *50* (40), 405102.
(47) Chava, V. S. N.; Barker, B. G.; Balachandran, A.; Khan, A.; Simin, G.; Greytak, A. B.; Chandrashekhar, M. V. S. High Detectivity Visible-Blind SiF_4 Grown Epitaxial Graphene/SiC Schottky Contact Bipolar Phototransistor. *Appl. Phys. Lett.* **2017**, *111* (24), 243504.
(48) Zheng, W.; Lin, R. C.; Jia, L. M.; Huang, F. Vacuum-Ultraviolet-Oriented Van Der Waals Photovoltaics. *Acs Photonics* **2019**, *6* (8), 1869.
(49) Kan, H.; Zheng, W.; Lin, R. C.; Li, M.; Fu, C.; Sun, H. B.; Dong, M.; Xu, C. H.; Luo, J. T.; Fu, Y. Q.; Huang, F. Ultra-Fast Photovoltaic-Type Deep-Ultraviolet Photodetector Using Hybrid Zero-/Two-Dimensional Heterojunctions. *ACS Appl. Mater.* **2019**, *11* (8), 8412.
(50) Kan, H.; Zheng, W.; Fu, C.; Lin, R. C.; Luo, J. T.; Huang, F. Ultrawide Band Gap Oxide Nanodots (E_g > 4.8 eV) for a High-Performance Deep Ultraviolet Photovoltaic Detector. *ACS Appl. Mater.* **2020**, *12* (5), 6030.
(51) Bencherif, H.; Dehimi, L.; Messina, G.; Vincent, P.; Pezzimenti, F.; Corte, F.G. D. An Optimized Graphene/4H-SiC/Graphene MSM UV-Photodetector Operating in a Wide Range of Temperature. *Sensor Actuat A-Phys.* **2020**, *307*, 112007.
(52) Zhang, Z.; Sun, C.; Zhu, B.; Chen, J.; Fu, Z.; Li, Z.; Wu, S.; Zhang, Y.; Cai, J.; Hong, R.; et al. High-Performance SiC/Graphene UV-Visible Band Photodetectors with Grating Structure and Asymmetrical Electrodes for Optoelectronic Logic Gate. *Adv. Opt. Mater.* **2024**, *12* (20), 2400469.
(53) Li, L.; Wei, G.; Zhu, P.; Su, Y.; Ding, L.; Ma, S.; Xu, B.; Wang, Y.; Yang, Y. Self-Powered Graphene/4H-SiC Nanowire Array-Based Ultraviolet Photodetectors with Fast Response Time and Low Dark Current for Promising Wireless Ultraviolet Communication. *Applied Materials Today* **2024**, *37*, 102114.
(54) Cherroun, R.; Meftah, A.; Sengouga, N.; Labed, M.; Kim, H.; Rim, Y. S.; Djemaa, A.; Meftah, A. Improvement of β-Ga_2O_3-Based Schottky Barrier UV Photodetector by 4H-SiC Substrate, Intrinsic Buffer Layer, and Graphene Surface Contact. *Journal of Materials Science: Materials in Electronics* **2024**, *35* (16), 1047.

https://doi.org/10.1021/acsanm.5c02220
ACS Appl. Nano Mater. 2025, 8, 15799−15807